Effects of pore fluid pressure on slip behaviors: An experimental study

A. Ougier-Simonin[1] and W. Zhu[1]

Received 8 March 2013; revised 3 May 2013; accepted 6 May 2013; published 7 June 2013.

[1] Slow slip behaviors are suggested to have a close correlation with the presence of excess pore fluid pressure. In this study, we conducted deformation experiments with and without excess pore pressure on intact porous sandstone samples to investigate effect of pore fluid pressure on rupture growth and slip instability. Experimental conditions are such that the samples failed either in brittle faulting or transitional regimes. The experimental results indicate that in the brittle faulting regime prone to seismic deformation, excess pore pressure causes reduction in brittle strength but no detectable difference in slip behavior compared to the cases without excess pore pressure. In the transitional regime, which is prone to stable deformation, excess pore pressure induces slip instability on otherwise stable sliding faults, but there are measurable differences compared to the unstable slip in the brittle faulting regime due to the interaction between unstable crack growth and dilatancy hardening. **Citation:** Ougier-Simonin, A., and W. Zhu (2013), Effects of pore fluid pressure on slip behaviors: An experimental study, *Geophys. Res. Lett.*, *40*, 2619–2624, doi:10.1002/grl.50543.

1. Introduction

[2] It has long been recognized that pore fluid pressure plays an important role in faulting processes [e.g., *Hubbert and Rubey*, 1959; *Secor*, 1965; *Davis et al*., 1983; *Johnson and McEvilly*, 1995]. The spatial and temporal variations in pore pressure distribution along faults likely control rupture nucleation and recurrence [e.g., *Sibson*, 1981; *Rice*, 1992; *Andrews*, 2002; *Segall et al*., 2010]. Because the shear strength of rocks obeys a law of effective stress [e.g., *Scholz*, 2002]—i.e. effective normal stress $\sigma_{eff} = \sigma_n - P_f$, where σ_n is the normal stress and P_f is the pore fluid pressure—decreases in effective normal stress due to increasing pore pressure can cause faults to slip at lower shear stresses. A classic example of high pore pressure induced fault slip is induced seismicity triggered by fluid injection [e.g., *Healy et al*., 1968; *Zoback and Harjes*, 1997].

[3] More recently, near lithostatic pore fluid pressure is linked to tectonic tremor activities observed at the down-dip of the subduction interface [e.g., *Obara*, 2002; *Shelly et al*., 2006]. Elevated pore pressure is also detected in the Nankai accretionary prism [e.g., *Saffer and Tobin*, 2011; *Kitajima and Saffer*, 2012] where very low frequency earthquakes (VLFE) and tectonic tremor occur [e.g., *Ito and Obara*, 2006; *Walter et al*., 2013] (Figure 1). Compared to regular earthquakes with similar magnitudes, the VLFEs and tectonic tremor have long rupture durations and are deficient in high-frequency energy. Seismic data suggest that VLFEs and tremor are manifestations of slow slip phenomena [e.g., *Ide et al*., 2007]. However, the underlying mechanisms of slip behaviors associated with VLFEs and tremors are unknown.

[4] Even though both fluid injection induced earthquakes and VLFEs are associated with elevated pore pressure, the differences in seismic signals indicate different rupture processes. Earthquake source mechanics models suggest that tectonic tremors and VLFEs arise from fault slip much slower than that of regular earthquakes. Numerical studies also showed that whether fault slip is slow or fast may depend on the competition between dilatant strengthening and thermal pressurization [e.g., *Segall et al*., 2010]. Many questions related to slow slip behaviors remain unclear. Does the transition of slip behavior from fast to slow take place in all rock types? What are the pressure, temperature, and fluid conditions for the transition to occur? How does the transition in slip behavior relate to the brittle-ductile transition in different rocks? Is near lithostatic pore pressure necessary for slow slip to occur [e.g., *Liu and Rice*, 2005]? If the slow slip behavior can be observed under controlled conditions in the laboratory, what would the fault plane look like? Is there microstructural evidence for competing deformation mechanisms as suggested?

[5] With these questions in mind, we conducted deformation experiments on intact rock samples to study the rupture nucleation and fault slip behaviors. We chose porous Berea sandstone because this rock undergoes the transition from the brittle faulting (i.e., fast slip) to cataclastic flow (i.e., no slip) through increasing confining pressures alone without elevated temperature [e.g., *Wong et al*., 1997]. Failure modes and slip behaviors in samples deformed at different confining pressures were investigated with and without the presence of elevated pore pressure. A slip-weakening model is used to describe the mechanics of fault slip [*Rice,* 1980]. Microstructural analyses were performed to elucidate the micromechanisms associated with slow slip behavior in this rock.

2. Material and Methods

[6] Berea sandstone used in this study consists of quartz, feldspar, carbonates, and clay minerals with a mean grain size of ~250 μm. All of the deformation tests were conducted at room temperature on water-saturated cylindrical cores with a length of 50.8 mm and a diameter

Additional supporting information may be found in the online version of this article.

[1]Department of Geology, University of Maryland, College Park, Maryland, USA.

Corresponding author: A. Ougier-Simonin, University of Maryland, 237 Regents Drive, College Park,MD, 20742, USA. (aougiers@umd.edu)

0094-8276/13/10.1002/grl.50543

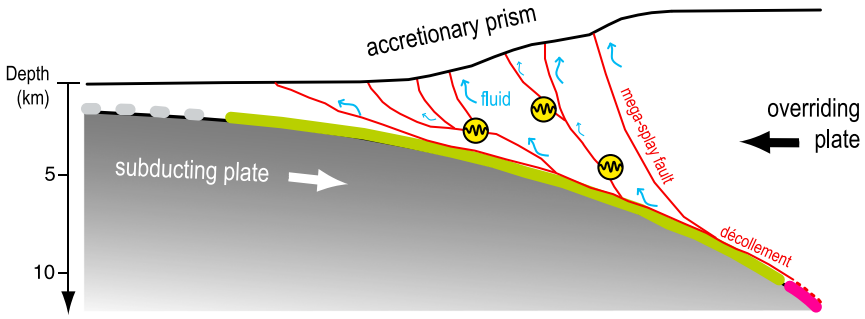

Figure 1. Conceptual diagram summarizing key fault slip processes and mechanical regime of deformation associated in accretionary subduction zone forearc. Dashed gray line illustrates the stable creeping zone where rocks are assumed to deform aseismically and/or in the ductile regime; solid green line points out the transitional zone of deformation where very low frequency earthquakes, tectonic tremor, and slow slips are schematically localized with sine waves in yellow circles (based on *Ito and Obara* [2006] and *Saffer and Tobin* [2011] works); solid magenta line indicates the extent of coseismic slip where rocks deformed in the brittle regime producing earthquakes.

of 25.4 mm. A constant strain rate of 3.5×10^{-6} s^{-1} was chosen to ensure ample time to maintain equilibration of pore pressure during stable deformation at the loading rate. With an initial porosity of ~21% and sufficiently high permeability (~10^{-13}–10^{-14} m^2) [e.g., *Zhu and Wong*, 1997], pore fluid pressure of the sample can be fully controlled through an external pressure intensifier during deformation. Confining pressures P_c were servo-controlled at 30 and 80 MPa, respectively. The maximum principal stress σ_1 was applied by an axial piston. With the axis-symmetric geometry, the intermediate and minimum stresses $\sigma_2 = \sigma_3$ (radial stresses). Axial (ε_α) and radial (ε_r) strains were recorded during deformation. Volumetric strain (ε_v) was subsequently calculated as $\varepsilon_v = \varepsilon_a + 2\varepsilon_r$.

[7] Two sets of deformation tests were conducted to investigate the effect of pore fluid pressure on slip behaviors (Table 1). In the first set (samples #1 and #3), the pore fluid pressure was kept constant at 10 MPa during deformation (i.e., constant pore fluid pressure "cPf" tests). In the second set (samples #2 and #4), pore pressure was kept constant only up to the onset of dilatancy C' (onset of inelastic deformation). Beyond C', pore fluid pressure was increased gradually while deformation continued (i.e., increasing pore fluid pressure "iPf" tests). The rate of pore pressure increase was chosen so that the nominal strain rate of 3.5×10^{-6} s^{-1} was maintained in the iPf tests. In the iPf tests, the final pore fluid pressures reached ~18–20 MPa. Differences in the effective mean stress $(p = ((\sigma_1 + \sigma_2 + \sigma_3)/3) - P_f$ and differential stress $(q = \sigma_1 - \sigma_3)$ between the cPf and iPf tests are shown in Figure S1 (supporting information).

3. Results

[8] The mechanical data are shown in Figure 2. We follow the convention that compressive stresses and compactive strains (i.e., shortening and volume decrease) are positive.

[9] Deformed at low confining pressure of $P_c = 30$ MPa, the inelastic behaviors and failure modes of samples #1 (cPf, red curves) and #2 (iPf, blue curves) were in the brittle faulting regime (Figures 2A and S1). The initial nonlinear strain response due to crack closure was followed by a linear elastic strain response with increasing differential stress. As deformation continued, the inelastic volume increase became non-negligible at C', the onset of dilatancy [*Brace et al.*, 1966]. A highly localized shear fracture developed after the differential stress reached its peak value (marked by a black arrow on Figure 2), followed by fault slip along the fracture (Figures 2A and 2C). In sample #1, the pore pressure was kept at 10 MPa throughout the test (cPf). In sample #2 (iPf), the pore pressure was increased (marked by a blue arrowhead with a water drop) from 10 to 20.5 MPa as deformation and brittle faulting took place. The peak stress of sample #2 is lower than that of sample #1, indicating a reduction in brittle shear strength due to excess pore pressure (Table 1 and Figure 2A). This result is consistent with the law of effective stress.

[10] Samples #3 and #4 were deformed at $P_c = 80$ MPa. Under cPf conditions, sample #30 failed by a diffuse damage zone instead of a highly localized shear fracture, and no fault slip was detected (Figures 2B and 2D). This indicates that the dynamic faulting process was prohibited by high confinements in this rock. Deformed at $P_c = 80$ MPa, Berea sandstone is in a transitional regime where the failure mode

Table 1. Summary of Experimental Conditions and Mechanical Data for all Samples

Sample	Type of Test	Confining Pressure (MPa)	Pore Pressure (MPa)	Peak Stress $\sigma_1 - \sigma_3$(MPa)	Fracture Angle (°)	Fault Width (mm)
#1	cPf[a]	30	10	64.3	34	0.30 ± 0.01
#2	iPf[a]	30	10 → 20.5	55	33	0.33 ± 0.01
#3	cPf[a]	80	10	91.4	52	3.19 ± 0.23
#4	iPf[a]	80	10 → 18	91.2	38	1.15 ± 0.41

[a]cPf = constant pore fluid pressure, iPf = increasing pore fluid pressure.

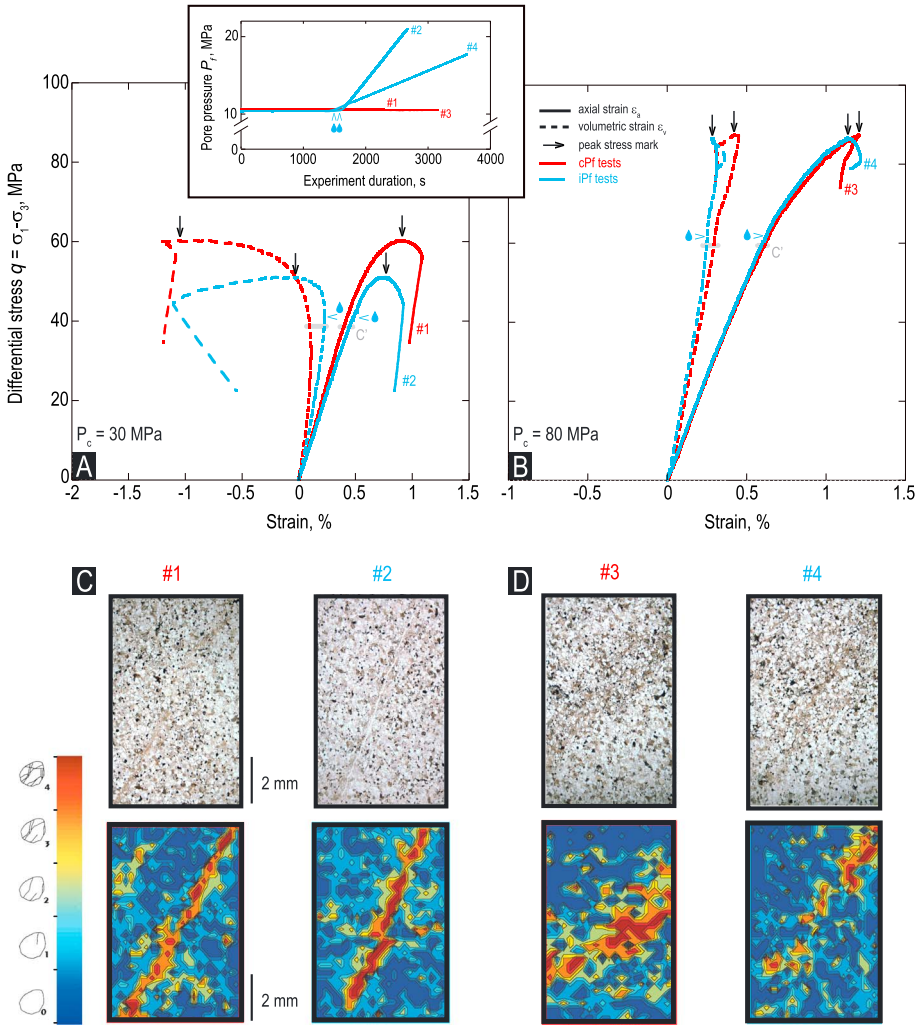

Figure 2. A–B) Mechanical data recorded for all experiments. Red curves are for constant pore pressure (cPf) tests, and blue ones for increasing pore pressure (iPf) tests. Axial (solid curves) and volumetric (dashed curves) strains show the damage history of the samples following the geological convention that shortening and compaction are positive, whereas elongation and dilation are negative. Onset of significant inelastic deformation C' is shown in light gray on the curves. Blue arrowheads with drops indicate the beginning of pore pressure increase for hp tests (which started after the onset of dilatancy); black arrows point the maximum differential stress. The insert shows the pore pressure as a function of time, where the values of the four experiments can be compared. C–D) Zoomed views on each sample thin sections and corresponding damage maps based on the microcrack density analysis. The correlation between the damage index and the color spectrum is plotted. Dark blue is for no inelastic damage (no intragranular cracks in grains) whereas dark red marks visible grain crushing; the spectrum of colors from dark blue to dark red characterizes increasing numbers of intragranular and transgranular cracks (based on *Tamarkin et al*. [2012]).

switches from the brittle faulting to the cataclastic flow [*Wong et al*., 1997]. Elastic moduli and shear strength of sample #4 (iPf, blue curves) are comparable to those of sample #3 (cPf, red curves), while the pore pressure increased from 10 MPa to ~18 MPa in sample #4 (Figure 2B and Table 1). Beyond the peak stress (pointed by a black arrow on Figure 2B), however, localized shear fracture was developed in sample #4 under iPf conditions (Figure 2D). The apparent difference in faulting at the transitional regime needs to be quantified now to understand the effect of excess pore pressure on slip behaviors.

[11] Microstructural analyses were conducted on the thin sections of the deformed samples. Intensive microcracking marks the microscale damage in all samples (Figure 2C). For samples #1 and #2 deformed at a low confining pressure ($P_c = 30$ MPa), coalescence and linkage of intensive microcracking form highly localized shear bands at similar angles of 34° and 33°, with respect to σ_1 (Figure 2C). Within the localized band, intensive microcracking is observed, in consistent with the dilatancy recorded (Figure 2A). The width of this band is similar for both samples, with respective values of 0.30 ± 0.01 and 0.33 ± 0.01 mm for samples #1 and #2 (Table 1). Deformed at a higher confinement ($P_c = 80$ MPa) and a constant pore pressure, sample #3 developed a diffuse damage zone at a much higher angle of ~52°. In comparison, the shear band in sample #4 deformed with increasing pore pressure is more localized at a more acute angle of 38° (Figure 2D). Clearly, increasing pore fluid pressure in sample #4 has promoted strain localization.

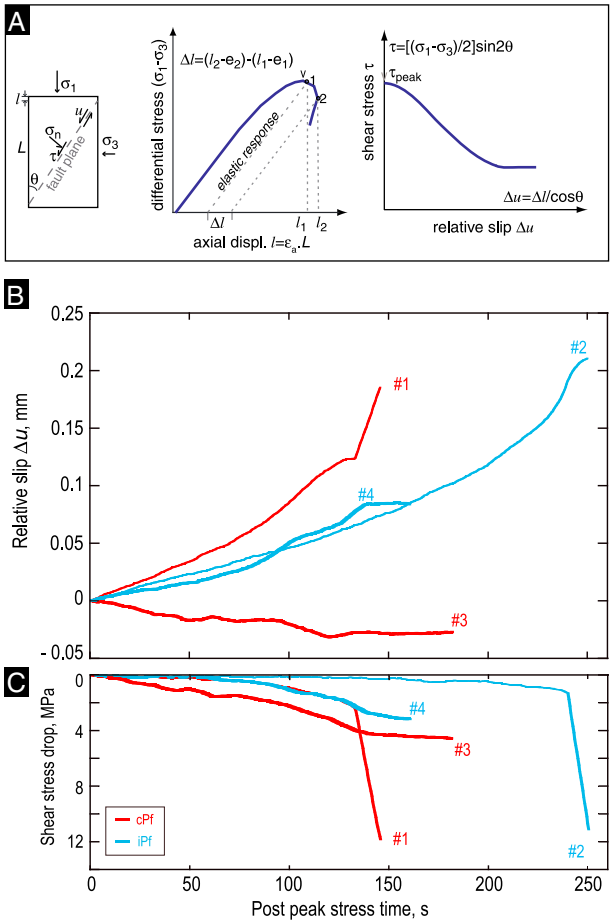

Figure 3. Plots of post-failure experimental data. A) Transformation of post-failure data illustrated with a schematic diagram of a fractured rock sample with initial length of L. Axial displacement l, effective normal stress σ_n, shear stress τ, and relative slip Δu along the fault plane can be derived from the axial strain ε_a, differential stress $\sigma_1 - \sigma_3$, and fracture angle θ. Post peak stress relative slip vs shear stress is then calculated and plotted. B) Relative slip along the fracture plane. Red and blue curves are for constant pore pressure (cPf) tests and increasing pore pressure (iPf) tests, respectively. C) Shear stress drop during the post-failure fault nucleation and propagation. See Table 1 for fracture angle values.

4. Dynamic Rupture Process and Slip-Weakening Model

[12] Compressive loading of initially intact rock commonly leads to the shear failure of rocks. Time-dependent crack growth results in dilatancy and increasing crack density during deformation. Crack interaction and coalescence eventually lead to the macroscopic shear fracture beyond peak stress. Following *Wong* [1982], the shear stress τ along the fault plane of angle θ with respect to σ_1 can be expressed as (Figure 3A):

$$\tau = \frac{1}{2}(\sigma_1 - \sigma_3)sin(2\theta). \quad (1)$$

[13] If the initial length of the sample is L, when the recorded axial strain is ε_a, the corresponding total axial displacement l is:

$$l = \varepsilon_a L. \quad (2)$$

[14] The total axial displacement l consists of both elastic strain component $e = E(\sigma_1 - \sigma_3)$ and the inelastic component (in forms of cracking in these tests). Young's modulus E can be derived from the portion of the stress-strain curve before the onset of dilatancy C' (Figure 2). Therefore, the inelastic displacement increment Δl between post-failure deformation stages 1 and 2 (as identified on Figure 3A) is:

$$\Delta l = (l_2 - e_2) - (l_1 - e_1). \quad (3)$$

[15] The relative slip Δu along the fault plane due to the inelastic deformation is (Figure 3A):

$$\Delta u = \frac{\Delta l}{cos\theta}. \quad (4)$$

[16] In a slip-weakening model [e.g., *Rice*, 1980], fracture nucleates when shear stress reaches the peak shear strength of a rock. As slip along the shear fracture increases, shear strength degrades (i.e., slip weakening). At a critical slip distance, frictional slip occurs for the fracture to propagate. Following this model, we analyzed the post peak stress slip behavior in our experiments.

[17] At the brittle faulting regime ($P_c = 30$ MPa), robust slip weakening is observed in both samples #1 and #2: shear

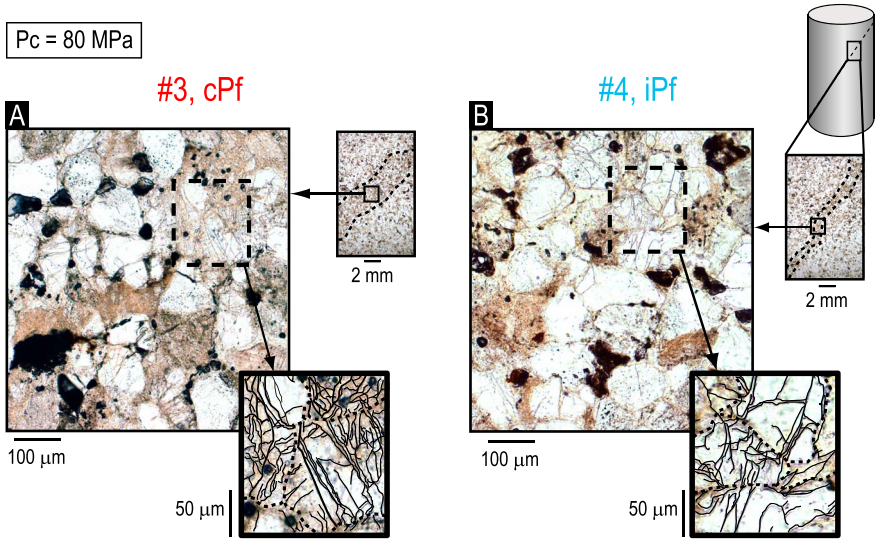

Figure 4. Micromechanisms of faulting observed in samples #3 and #4 deformed at a confining pressure $P_c = 80$ MPa and with constant (cPf) and increasing (iPf) pore pressure. Black solid lines in the biggest zoomed views mark the microcracks identified in grains; dashed black lines underline the grain contours.

stress along faults decreases as slip along shear fracture increases (Figure 3B). The slip behaviors for both samples can be described by increasing slip rate (i.e., relative slip curves with increasing slopes) accompanied by continuous stress drops, suggesting velocity-weakening behaviors (Figures 3B and 3C). Slip rates are comparable in samples with (in sample #2) and without (in sample #1) excess pore pressure (Figure S2). In other words, the presence of excess pore fluid pressure does not have a detectable effect on fault slip behavior in the brittle faulting regime.

[18] At the transitional regime ($P_c = 80$ MPa), sample #3 deformed at constant pore pressure developed a diffuse damage zone. The calculated relative slip Δu in sample #3 is negligible (Figure 3B), indicating that dynamic faulting is prohibited at high confinement, and the slip is stable. In contrast, deformed under increasing pore pressure, sample #4 developed a more localized shear band (2D). The relative slip along fault in sample #4, while less than those in samples #1 and #2, is considerable (Figure 3B). Unlike in samples #1 and #2 where slip rates accelerate during faulting, slip rate increase in sample #4 is not robust, with several flat periods (Figure 3B). This suggests that the fault in sample #4 is only borderline velocity weakening. The maximum slip rate in sample #4 is much smaller than those in samples #1 and #2 (Figure S2). Furthermore, the shear stress drop in sample #4 during slip weakening is very small compared to those in samples #1 and #2. Overall, the experimental data indicate that in the transitional regime, excess pore pressure enhances slip instability along an otherwise aseismic fault, but the slip behavior is markedly different from the brittle faulting.

5. Discussion

[19] The micromechanisms involved in our experiments are primarily Hertzian contact cracking (Figure 2C). Detailed microstructural analysis reveals that the zone of diffuse damage (~3.19 ± 0.23 mm in width) in sample #3 consists of highly cracked grains (as an example, more than 20 intragranular cracks can be identified in each grain on Figure 4A). Clearly, high confinements impede crack growth; faulting was replaced by pervasive sub-critical crack ultimately leading to a diffuse damage zone in "cPf" sample #3. In comparison, deformed at the same confinement but with increasing pore pressure, the shear band in sample #4 is much more localized (~1.15 ± 0.41 mm in width). The intragranular density within the shear band is considerably lower (Figure 4B). An intuitive explanation is that the excess pore pressure in sample #4 reduces the effective normal stress and thus enhances fault growth.

[20] Under compressive loading, cracking can cause dilatancy-induced suction in a fluid-saturated rock, which increases effective normal stress on the crack surfaces and thus impedes further crack growth. This phenomenon is referred to as dilatancy hardening [e.g., *Rice*, 1975]. Whether the impeding effect of dilatancy hardening is significant depends on the fluid diffusion processes. If the permeability is high and the pore pressure re-equilibration (under fully drained conditions) is fast compared to the faulting process, dilatancy hardening effect on fault slip would be negligible. Otherwise, dilatancy hardening could play an important role in the faulting process. Dilatancy hardening likely impedes faulting in the transitional regime, thus results in the observed slow slip behavior in sample #4. Because the fault zone permeability at low confining pressure is likely higher, effect of dilatancy hardening on fault slip in samples #1 and #2 is negligible.

6. Concluding Remarks

[21] The mechanical data presented in this study demonstrate that excess pore fluid pressure enhances seismicity by lowering the shear strength of rocks. In the brittle faulting regime, fault slip associated with excess pore pressure is qualitatively similar to that without excess pore pressure. At the transitional regime where dynamic faulting is prohibited, excess pore pressure enhances slip instability, but the slip behavior is quite different from slip along a brittle fault. Our experimental data also show that the maximum

overpressure does not need to be near-lithostatic to induce slow slip in the sandstone samples studied here. In this study, the deformation mechanism that controls such transitional slip behavior is the interaction between unstable crack growth and dilatancy hardening.

[22] It is worthwhile to emphasize that these experiments do not simulate the slip events in the field. The rock types, strain rates, environmental conditions, and interstitial fluid compositions vary greatly at different geological settings. For other rocks, deformation mechanisms associated with slow slip are expected to be different. However, despite these differences, the prevalence of slow slips suggests that this transitional fault slip is a common feature. Conditions at both the up-dip and down-dip regions in subduction zones seem to satisfy the two requirements for slow slip to occur: presence of excess pore pressure and a brittle-ductile transitional regime [*Dragert et al*., 2004]. Thus, it is not surprising that slow slip events are primarily detected in these regions. In comparison, the conditions at the locked seismogenic region would not favor slow slip even if pore pressure buildup occurs. Below the down-dip region, localized fault is inhibited due to high pressure and temperature, deformation is dominantly plastic flow that is insensitive to pressure change.

[23] **Acknowledgments.** Partial support from the National Science Foundation through a CAREER grant NSF-EAR1056317 and the Department of Energy through grant DE-FG02-07ER15916 are acknowledged. Technical support from Ted Koczynski and Thomas Tamarkin is greatly appreciated. We thank Sarah Penniston-Dorland for her assistance in the optical microscopy lab.

References

Andrews, D. J. (2002), A fault constitutive relation accounting for thermal pressurization of pore fluid, *J. Geophys. Res.*, *107*(B12), 2363, doi:10.1029/2002JB001942.

Brace, W. F., B. W. Paulding Jr., and C. H. Scholz (1966), Dilatancy in the fracture of crystalline rocks, *J. Geophys. Res.*, *71*, 3939–3953.

Davis, D., J. Suppe, and F. Dahlen (1983), The mechanics of foldand thrust belts and accretionary wedges, *J. Geophys. Res.*, *88*, 1153–1172.

Dragert, H., K. Wang, and G. Rogers (2004), Geodetic and seismic signatures of episodic tremor and slip in the northern Cascadia subduction zone, *Earth Planets Space*, *56*, 1143–1150.

Healy, J. H., W. W. Rubey, D. T. Griggs, and C. B. Raleigh (1968), The Denver Earthquakes, *Science*, *161*, 1301–1310, doi:10.1126/science.161.3848.1301.

Hubbert, M., and W. Rubey (1959), Role of fluid pressure in mechanics of overthrust faulting, pt. i, mechanics of fluid-filled porous solids and its application to overthrust faulting, *Geol. Soc. Am. Bull.*, *70*, 115–166.

Ide, S., D. Shelly, and G. Beroza (2007), Mechanism of deep low frequency earthquakes: further evidence that deep non-volcanic tremor is generated by shear slip on the plate interface, *Geophys. Res. Lett.*, *34*, L03308, doi:10.1029/2006GL028890.

Ito, Y., and K. Obara (2006), Very low frequency earthquakes within accretionary prisms are very low stress-drop earthquakes, *Geophys. Res. Lett.*, *33*, L09302, doi:10.1029/2006GL025883.

Johnson, P. A., and T. V. McEvilly (1995), EParkfield seismicity: fluid-driven?, *J. Geophys. Res.*, *100*, 12,937–12,950, doi:10.1029/95JB00474.

Kitajima, H., and D. M. Saffer (2012), Elevated pore pressure and anomalously low stress in regions of low frequency earthquakes along the Nankai Trough subduction megathrust, *Geophys. Res. Lett.*, *39*, L23301, doi:10.1029/2012GL053793.

Liu, Y., and J. R. Rice (2005), Aseismic slip transients emerge spontaneously in 3D rate and state modeling of subduction earthquake sequences, *J. Geophys. Res.*, *110*, B08307, doi:10.1029/2004JB003424.

Obara, K. (2002), Nonvolcanic deep tremor associated with subduction in southwest Japan, *Science*, *296*, 1679–1681.

Rice, J. R. (1975), On the stability of dilatant hardening for saturated rock masses, *J. Geophys. Res.*, *80*, 1531–1536.

Rice, J. R. (1980), The mechanics of earthquake rupture, in *Physics of the Earth's Interior*, (Proc. International School of Physics 'Enrico Fermi', Course 78, 1979; ed. A. M. Dziewonski and E. Boschi), Italian Physical Society, Bologna, and North-Holland Publ. Co., Amsterdam, pp. 555–649

Rice, J. R. (1992), Fault stress states, pore pressure, distributions, and the weakness of the San Andreas fault, in *Fault mechanics and transport properties of rocks*, Evans, B., and Wong, T. F., eds., New York, Academic Press, pp. 475–504.

Saffer, D., and H. Tobin (2011), Hydrogeology and mechanics of subduction zone forearcs: fluid flow and pore pressure, *Annu. Rev. Earth Planet. Sci.*, *39*, 157–186.

Scholz, C. (2002), *The Mechanics of Earthquakes and Faulting*, Cambridge university press, United Kingdom, 2nd edition, 471 pp.

Secor, D. (1965), Role of fluid pressure in jointing, *Am. J. Sci.*, *263*, 633–646.

Segall, P., A. M. Rubin, A. M. Bradley, and J. R. Rice (2010), Dilatant strengthening as a mechanism for slow slip events, *J. Geophys. Res.*, *115*, B12305, doi:10.1029/2010JB007449.

Shelly, D., G. Beroza, S. Ide, and S. Nakamula (2006), Low-frequency earthquakes in Shikoku Japan, and their relationship to episodic tremor and slip, *Nature*, *442*, 188–191.

Sibson, R. H. (1981), Fluid flow accompanying faulting: field evidence and models, D.W. Simpson and P.G. Richards (Editors), Earthquake Prediction: An international Review, *Am. Geophys. Union Maurice Ewing Vol.*, *4*, 593–603.

Tamarkin, T., A. Ougier-Simonin, and W. Zhu (2012), Progressive microscopic damage associated with fault growth, *Geophys. Res. Lett.*, *39*, L15303, doi:10.1029/2012GL052487.

Walter, J. I., S. Y. Schwartz, M. Protti, and V. Gonzalez (2013), The synchronous occurrence of shallow tremor and very low frequency earthquakes offshore of the Nicoya Peninsula Costa Rica, *Geophys. Res. Lett.*, *16*, 1517–1522, doi:10.1002/grl.50213.

Wong, T.-F. (1982), Shear fracture energy of Westerly granite from post-failure behavior, *J. Geophys. Res.*, *87*, 990–1000.

Wong, T.-F., C. David, and W.-l. Zhu (1997), The transition from brittle faulting to cataclastic flow in porous sandstone: mechanical deformation, *J. Geophys. Res.*, *102*, 3009–3025.

Zoback, M. D., and H.-P. Harjes (1997), Injection-induced earthquakes and crustal stress at 9 km depth at the KTB deep drilling site, Germany, *J. Geophys. Res.*, *102*, 18,477–18,491.

Zhu, W., and T.-f. Wong (1997), The transition from brittle faulting to cataclastic flow: Permeability evolution, *J. Geophys. Res.*, *102*, doi:10.1029/96JB03282.